ADVANCED MATERIALS
www.advmat.de

Transforming the Chemical Structure and Bio-Nano Activity of Doxorubicin by Ultrasound for Selective Killing of Cancer Cells

Sukhvir Kaur Bhangu, Soraia Fernandes, Giovanni Luca Beretta, Stella Tinelli, Marco Cassani, Agata Radziwon, Marcin Wojnilowicz, Sophia Sarpaki, Irinaios Pilatis, Nadia Zaffaroni, Giancarlo Forte, Frank Caruso, Muthupandian Ashokkumar,* and Francesca Cavalieri**

Reconfiguring the structure and selectivity of existing chemotherapeutics represents an opportunity for developing novel tumor-selective drugs. Here, as a proof-of-concept, the use of high-frequency sound waves is demonstrated to transform the nonselective anthracycline doxorubicin into a tumor selective drug molecule. The transformed drug self-aggregates in water to form ≈200 nm nanodrugs without requiring organic solvents, chemical agents, or surfactants. The nanodrugs preferentially interact with lipid rafts in the mitochondria of cancer cells. The mitochondrial localization of the nanodrugs plays a key role in inducing reactive oxygen species mediated selective death of breast cancer, colorectal carcinoma, ovarian carcinoma, and drug-resistant cell lines. Only marginal cytotoxicity (80–100% cell viability) toward fibroblasts and cardiomyocytes is observed, even after administration of high doses of the nanodrug (25–40 μg mL^{-1}). Penetration, cytotoxicity, and selectivity of the nanodrugs in tumor-mimicking tissues are validated by using a 3D coculture of cancer and healthy cells and 3D cell-collagen constructs in a perfusion bioreactor. The nanodrugs exhibit tropism for lung and limited accumulation in the liver and spleen, as suggested by in vivo biodistribution studies. The results highlight the potential of this approach to transform the structure and bioactivity of anticancer drugs and antibiotics bearing sono-active moieties.

1. Introduction

Nanodrugs often combine the functionality of an active therapeutic agent and a nanoscale carrier to control the pharmacokinetics, biodistribution, and cellular targeting of drugs in tumors, while limiting cytotoxic effects in healthy tissues.[1] The development of either new drugs or nanodrugs from in silico design to clinical trials, remains challenging, lengthy, and costly, with a high degree of uncertainty for the new therapeutic agents to reach the market and ultimately benefit patients.[2] Most chemotherapeutic nanodrugs in clinical trials or approved for use are based on lipids or micellar formulations and incorporate standard off-patent anticancer agents such as doxorubicin (DOX), irinotecan, paclitaxel, and cisplatin.[3] Advanced and sophisticated nanocarriers like carbon- and polymer-based nanoparticles, mesoporous inorganic materials, metal–organic frameworks, and DNA and

S. K. Bhangu, F. Cavalieri
School of Science
RMIT University
Melbourne, Victoria 3000, Australia
E-mail: francesca.cavalieri@unimelb.edu.au
S. K. Bhangu, A. Radziwon, M. Wojnilowicz, F. Caruso
Department of Chemical Engineering
The University of Melbourne
Parkville, Victoria 3010, Australia
S. K. Bhangu, M. Ashokkumar
School of Chemistry
The University of Melbourne
Victoria 3010, Australia
E-mail: masho@unimelb.edu.au
The ORCID identification number(s) for the author(s) of this article can be found under https://doi.org/10.1002/adma.202107964.

DOI: 10.1002/adma.202107964

S. Fernandes, M. Cassani, G. Forte
International Clinical Research Center (ICRC)
St Anne's University Hospital
Brno 65691, Czechia
G. L. Beretta, S. Tinelli, N. Zaffaroni
Molecular Pharmacology Unit
Department of Applied Research and Technological Development
Fondazione IRCCS Istituto Nazionale dei Tumori di Milano
Via Amadeo 42, Milan 20133, Italy
E-mail: giovanni.beretta@istitutotumori.mi.it
S. Sarpaki, I. Pilatis
BIOEMTECH
27 Neapoleos st., Lefkippos Attica Technology
Park - N.C.S.R. Demokritos, Athens 15341, Greece
F. Cavalieri
Dipartimento di Scienze e Tecnologie Chimiche
Università degli Studi di Roma "Tor Vergata"
via della ricerca scientifica 1, Rome 00133, Italy

RNA nanostructures are under investigation for the delivery of conventional anticancer drugs.[4] In these systems, the encapsulated drugs typically exhibit the same mechanism of action along with collateral toxicity (i.e., drug resistance and cardiotoxicity) as the nonformulated drugs. In addition, the nanocarrier components (polymers, lipids, proteins, nucleic acids, and oxides)[2,5] can exhibit immunological activity, for instance, the induction of complement-mediated infusion reactions or the activation of proinflammatory cytokines has been reported.[6] A way to improve the safety and efficacy of anticancer nanodrugs is to remove the need for a carrier and engineer nanodrugs composed entirely of the active-molecules. Compared to small molecule therapeutics, nanodrugs solely made of drug molecules carry a higher dose of chemotherapeutics. Carrier-free nanodrugs and nanocrystals based on molecular self-assembly of drug molecules were recently developed by organic solvent-exchange methods for in vitro and in vivo cancer therapy.[7,8] However, these methods require the chemical modification of drugs with fatty acids, photosensitizer, crosslinkers, and ligands[7,8] and stabilizing agents such as surfactants or polyethylene glycol.[8]

To substantially advance this field, the development of simple, scalable, and cost-effective methods for the transformation of "conventional molecular drugs" into nanodrugs is of paramount importance. Furthermore, an alternative approach to control the subcellular location of nanodrugs in cancer cells without resorting to targeting ligands is also desirable for selectively killing of different types of cancer cells.

Herein, we show that high-frequency sound waves in aqueous solution can induce the transformation and self-assembly of a traditional anthracycline, DOX, into a new class of carrier-free nanodrug. Unlike other reported methods, this approach does not require organic solvents or chemical agents to induce the chemical modification, self-assembly and colloidal stabilization of nanodrugs. The obtained nanodrug exhibits reactive oxygen species (ROS)-mediated cytotoxicity on human breast cancer, colorectal carcinoma, ovarian carcinoma, and drug-resistant cell lines, whereas limited cytotoxicity toward fibroblasts and cardiomyocytes was observed. Single-molecule localization and confocal microscopy enabled probing of intracellular trafficking, disassembly, and subcellular localization of the nanodrug, with nanoscale resolution. While DOX molecules accumulated in the cell nuclei and induced DNA damage in cancer cells, healthy fibroblasts, and cardiomyocytes, the transformed drug showed preferential affinity for lipid raft domains, which are abundant in the mitochondria of cancer cells. Consequently, the generation of ROS caused DNA damage and triggered the selective death of cancer cells. The cytotoxicity and selectivity of the nanodrug was also validated using 3D cocultures of cancer cells and healthy fibroblasts under static conditions, in the form of spheroids, and 3D cells-collagen constructs under U-Cup perfusion bioreactor. The in vivo biodistribution study revealed a preferential accumulation of the nanodrug in the lungs of healthy mice and a lack of toxicity over 10 days post-intravenous injection. Our results highlight the utility of the developed nanodrug as a versatile and promising platform for selective killing of cancer cells.

This simple approach can be potentially extended to other commercial anticancer drugs (e.g., mitoxantrone, epirubicin, daunorubicin, etc.) and antibiotics (e.g., doxycycline, sarecycline, tetracycline, etc.) bearing sono-active moieties such as phenolic, quinone, and aromatic groups to generate new pharmacoactive molecules that may readily self-assemble into supramolecular carrier-free nanodrugs.

2. Results and Discussion

2.1. Ultrasound-Driven Self-Assembly of DOX into Nanodrugs

A nanodrug made of chemically modified DOX molecules, hereafter referred to as doxorubicin nanodrug (ND_{DOX}) was prepared by the recently established ultrasound-driven self-assembly method (**Figure 1a**).[9,10]

Our fundamental studies[9,10] have revealed that the oscillating surface of acoustic cavitation microbubbles acts as a reactive and catalytic site for the C—C coupling of amphiphilic aromatic molecules. The oscillating bubbles, driven by the high frequency acoustic field, provide a transient liquid–air interface where the chemically modified amphiphilic molecules are collected. Upon bubble collapse, the self-assembly of the amphiphilic molecules into nanoparticles is observed as result of the high local concentration, high shear stress, and strong intermolecular interactions between the amphiphilic aromatic molecules. It was established[9,10] that 300–500 kHz is the optimal ultrasound frequency range to generate enough •OH radicals to induce hydroxylation and dimerization of the aromatic molecules. The dynamic behavior and lifetime (0.3–0.1 ms) of cavitation bubbles driven at high frequency is important to enable the diffusion of molecules at the air–liquid interface before bubble collapse.[10] Low frequency ultrasound (20 kHz) and very high frequency (>1 MHz) were found ineffective in the formation of dimers and nanoparticles due to low amount of •OH radicals generated.[10] In this study the 490 kHz frequency was chosen as this condition provides optimal chemical and physical effects for the chemical transformation of doxorubicin and ND_{DOX} formation, as shown in Figure 1.

As shown in Figure 1, the acoustic cavitation generated by high-frequency (490 kHz) ultrasound induces structural changes in the amphiphilic aromatic molecules (Figure 1a-i) adsorbed at the transient cavitation bubble/solution interface (Figure 1a-ii). The amphiphilic molecules ultimately self-assemble into nanoparticles (Figure 1a-iii) during bubble collapse due to intermolecular interactions, i.e., H-bonding and π–π interactions.[9,10] The ND_{DOX} particles have a spherical morphology with an average diameter of 193 ± 56 nm in the hydrated state, as determined using super-resolution stochastic optical reconstruction microscopy (STORM) (Figure 1b and Figure S1a, Supporting Information). The spherical morphology of ND_{DOX} was also confirmed by atomic force microscopy (AFM), scanning electron microscopy (SEM), and transmission electron microscopy (TEM) images (Figure 1c–e). The hydrodynamic diameter of particles was ≈275 ± 108 nm (polydispersity Index, PDI = 0.202), as determined by dynamic light scattering, DLS (Figure 1f). The drying process induced a significant size shrinkage of ND_{DOX} to ≈90 ± 30 nm, as determined by AFM, SEM, and TEM. This suggests that the self-assembly of the amphiphilic molecules results in the formation

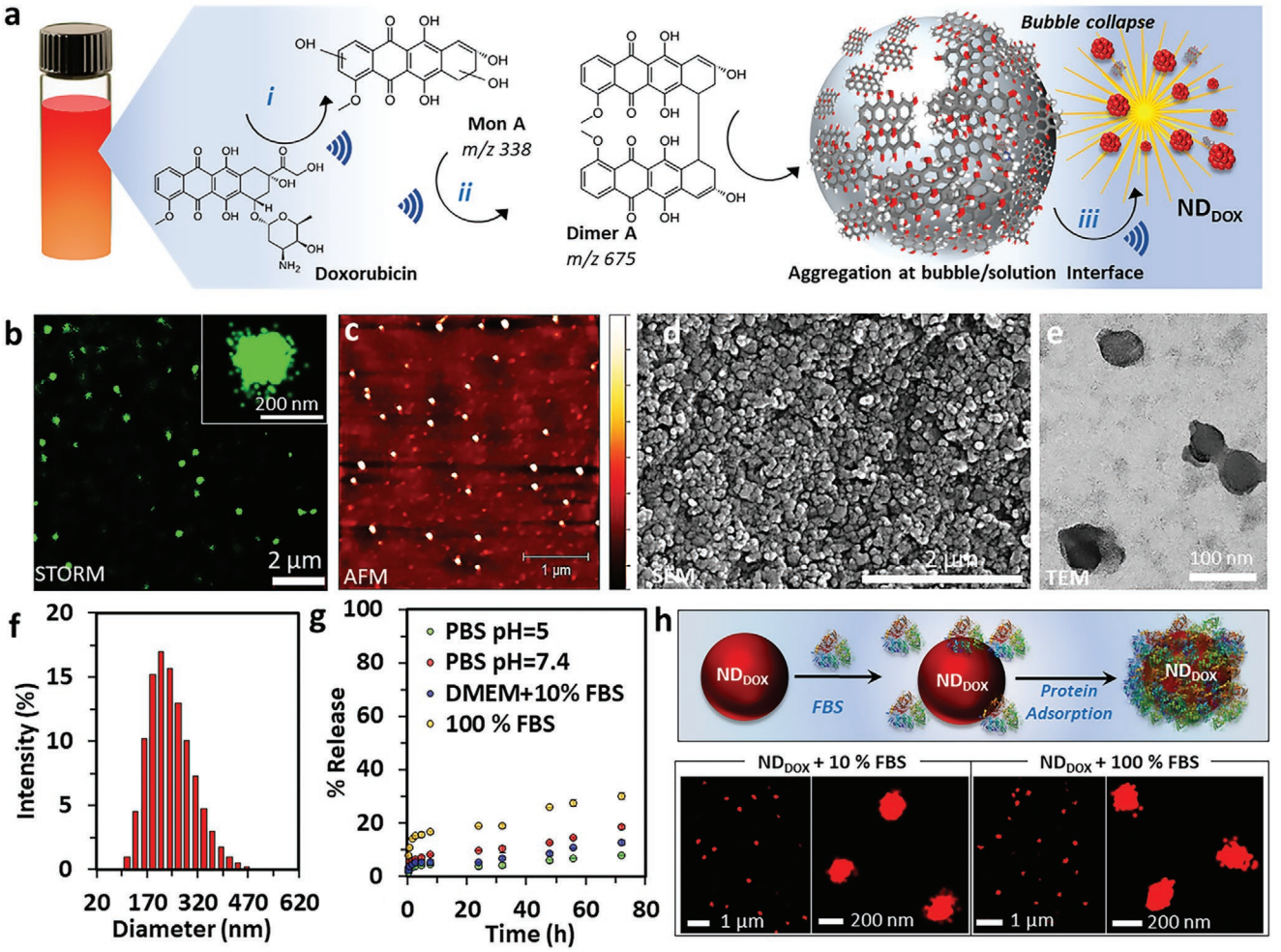

Figure 1. Engineering DOX into a stable nanodrug. a) Schematic of the ultrasound-assisted engineering of DOX into ND$_{DOX}$. A solution of DOX in water (0.5 mg mL^{-1}) was sonicated at high frequency (490 kHz) and 2 W cm^{-2} for 3 h to readily form ND$_{DOX}$. DOX is converted into hydroxylated species (MonA and DimA) (i) at the transient cavitation bubble/solution interface (ii) and subsequently the products self-assemble upon bubble collapse to form uniform ND$_{DOX}$ nanoparticles (iii). b) Representative STORM image of ND$_{DOX}$ labeled with the photoswitchable dye AF 647; the inset shows a magnified view of a single ND$_{DOX}$ nanoparticle. The results are from three independent experiments. c) AFM (height 0–10 nm), d) SEM, and e) TEM images of ND$_{DOX}$ nanoparticles, respectively. f) The size distribution of ND$_{DOX}$ in aqueous solution, determined using DLS. g) Dissolution kinetics of ND$_{DOX}$ at pH 5 and pH 7.4 in 100 × 10^{-3} M PBS, 100% FBS, and cell culture medium Dulbecco's modified Eagle medium containing 10% FBS. The % release was determined by measuring fluorescence emission (λ_{520nm}) of the collected supernatant after centrifugation of ND$_{DOX}$. h) Scheme showing the adsorption of protein on the surface of ND$_{DOX}$ after incubation with FBS and STORM images of the ND$_{DOX}$ acquire after 8 h incubation with 10% and 100% FBS. Results are from three independent experiments.

of a hydrated physical network. The ND$_{DOX}$ particles displayed similar absorption and fluorescence emission properties to DOX within the orange-red region of the spectrum (Figure S1b,c, Supporting Information). Mass spectrometry analysis of the disassembled ND$_{DOX}$ (Figure S2, Supporting Information) revealed the presence of a high molecular weight dimer (DimA; m/z 675) and hydroxylated monomers (MonA; m/z 376, 392, 408) likely arising from fragmentation of dimers. High-performance liquid chromatography (HPLC) analysis (Figure S3, Supporting Information) of ND$_{DOX}$ dissolved in water suggested that most of the particles were composed of a single species in addition to slight amount of low- and high-molecular-weight species. Since cavitation bubbles generate OH radicals in aqueous solutions,[11] our data suggest that the radical-mediated oxidation of DOX results in the cleavage of the hydroxyacetyl and aminoglycoside moieties to form a new derivative, MonA, (Figure 1a and Figure S2, Supporting Information), which undergoes dimerization (Figure 1a and Figure S2, Supporting Information) by self-coupling reactions to ultimately form DimA. The NMR and Fourier transform infrared spectra of ND$_{DOX}$ (Figure S4a,b, Supporting Information) confirmed the chemical modification and hydroxylation of the aromatic moieties. The ND$_{DOX}$ particles had a ζ-potential of −25 ± 8 mV, remain stable as a dispersion for at least one year and can be also stored as redispersible dry powder without adding surfactants.

The stability of ND$_{DOX}$ in solutions mimicking physiological conditions was studied by monitoring the dissolution of the nanoparticles as a function of time. After 30 h incubation, slight dissolution of ND$_{DOX}$ was observed in phosphate

buffered saline (PBS) at pH 5 (4%), pH 7 (8%), in cell culture medium (6%), and 100% fetal bovine serum, FBS, (16%) (Figure 1g). The deprotonation of OH groups of the polyhydroxylated aromatic molecules at neutral pH likely promotes the slow disassembly of ND_{DOX} at equilibrium because of repulsive electrostatic interactions between the negatively charged drug molecules.[12] These results indicate that ND_{DOX} particles are stable in biological media and disassemble gradually over a prolonged period of time. To give an insight into the interactions between ND_{DOX} and serum proteins, ND_{DOX} were mixed with different concentrations of FBS and directly analyzed by STORM microscopy, particle tracking analysis and sodium dodecyl sulfate–polyacrylamide gel electrophoresis, (SDS–PAGE). Notably, the presence of serum proteins in phosphate-buffered saline solution (10% and 100% FBS) did not cause aggregation or significant dissolution of ND_{DOX} over an observation period of 8 h, as indicated by STORM imaging (Figure 1h) and particle tracking analysis (Videos S1 and S2, Supporting Information). However, ND_{DOX} showed a slight decrease in ζ-potential (–16 ± 5 mV) upon incubation with 100% FBS indicating the presence of a protein corona which is likely mediated by electrostatic or hydrophobic interactions. The absorption of serum proteins particularly albumin on the surface of ND_{DOX} was confirmed using SDS–PAGE (Figure S4c, Supporting Information). Nevertheless, ND_{DOX} particles remain associated in serum and can potentially access the lesion sites, after in vivo injections, by crossing the endothelial cells through an active process of transcytosis[13] or by the passive enhanced permeability and retention effect.[14]

Overall, these results indicated that the chemical structure of doxorubicin and its supramolecular assembly properties can be transformed by a simple and reagent-less ultrasonic treatment, performed in aqueous environment, to potentially obtain carrier-free nanodrugs.

2.2. ND_{DOX} Exerts ROS-Mediated Cytotoxicity on Drug-Resistant Tumor Cell Lines

The anticancer activity of ND_{DOX} was evaluated on human cancer cell lines of different tumors, including human breast cancer (MDA-MB-231), colorectal carcinoma (LoVo), and ovarian carcinoma (A2780) cell lines. In addition, the ability of ND_{DOX} to circumvent drug resistance was evaluated using DOX-resistant colorectal (LoVo/DX) and ovarian carcinoma (A2780/DX) cell line variants. These two variants express high levels of P-glycoprotein, a membrane ATP-binding cassette transporter, implicated in the efflux of different drugs, including DOX, which is known to contribute to cellular drug resistance.[15] ND_{DOX} maintained antiproliferative activity in MDA-MB-231 cells and this effect is enhanced at prolonged exposure times (**Figure 2**a). The antiproliferative activity of ND_{DOX}, measured as the concentration of drug required to induce 50% cell growth reduction (IC_{50} = 16 μg mL^{-1}, 48 h, Figure 2a), was 30 times lower than that of DOX (IC_{50} = 0.5 μg mL^{-1}, 48 h) (Figure 2b). The apparent lower toxicity of the ND_{DOX} can be attributed to its slower cellular uptake and dissolution, which can affect the availability of DimA compared to free DOX, which is rapidly uptaken by passive diffusion and immediately bound by DNA in the nucleus (Figure 2c). This was verified by comparing the cytotoxicity of DOX and ND_{DOX} following dissolution after 48 h incubation. In its soluble form DimA (IC_{50} = 3 μg mL^{-1}) exhibited only six times lower toxicity compared to DOX (IC_{50} = 0.5 μg mL^{-1}), confirming our hypothesis (Figure 2b). Additionally, after 72 h incubation with colorectal (LoVo) and ovarian carcinoma (A2780) cells, (Figure S5a,b and Table S1, Supporting Information), ND_{DOX} appeared 10–40-fold less cytotoxic than DOX.

Furthermore, ND_{DOX} showed a lower resistance index, *R*, than DOX in both drug-sensitive and resistant cell lines (*R* is defined as the ratio of the IC_{50} values of the drug-resistant and sensitive cells) (Figure S5c, Supporting Information). Specifically, *R* of ND_{DOX} was ≈2.5× lower than *R* of DOX after exposure for 2 and 72 h in A2780–A2780/DX cell lines (Figure S5c, Supporting Information). This behavior was also observed in LoVo–LoVo/DX cell lines (19× and 1.2× lower at 2 and 72 h exposure, respectively). The lower *R* observed suggests that ND_{DOX} can potentially circumvent the mechanism of drug resistance activated by cells.

Overall a reduction in potency of ND_{DOX} was observed compared to DOX; however, this is likely dependent on the different mechanisms of action of the two drugs and the dissolution kinetics of ND_{DOX}. It is worth noting that in the rational design of new nanodrugs for cancer therapy the main goal is to kill cancer cells but equally important is to reduce the toxic side effects such as nonselective toxicity (cardiotoxicity) and drug resistance.

Next, the mechanism of action underlying the anticancer effect and selectivity of the engineered ND_{DOX} was investigated. The biological activity of ND_{DOX} is primarily dependent on its cellular uptake, intracellular trafficking, and subcellular localization. The main mechanism of action of anthracyclines entails the intercalation of the drug into double-stranded DNA, resulting in inhibition of DNA replication and transcription as well as topoisomerase II (TopoII) activity by locking the enzyme into a cytotoxic DNA cleavable complex.[16,17] In addition, anthracyclines instigate the generation of ROS, which causes oxidative stress and ultimately cell death by apoptosis or necrosis.[18,19] Confocal microscopy images of MDA-MB-231 cells incubated with DOX for 24 h at 37 °C show that DOX was exclusively accumulated in the cell nuclei (Figure 2c). On the contrary, ND_{DOX} (Figure 2d) and the released drug molecules did not show any nuclear accumulation and were confined within other cellular compartments primarily located in the peri-nuclear region.

It is worth noting that DimA molecules (Figure 1a) lack the glucose moiety, which is vital for poisoning the TopoII–DNA cleavable complex.[20] Moreover, DimA molecules are likely too bulky to intercalate into double-stranded DNA. To confirm this hypothesis, a plasmid DNA gel-retardation assay using agarose gel electrophoresis was performed (Figure 2e). The migration of DNA exposed to DimA or DOX was compared with that of control DNA. We observed that the migration of plasmid DNA exposed to DimA was similar to that of control DNA, whereas DOX and ethidium bromide had a significant impact on DNA plasmid migration. Confocal microscopy and DNA gel-retardation assay results confirm the hypothesis that TopoII-mediated

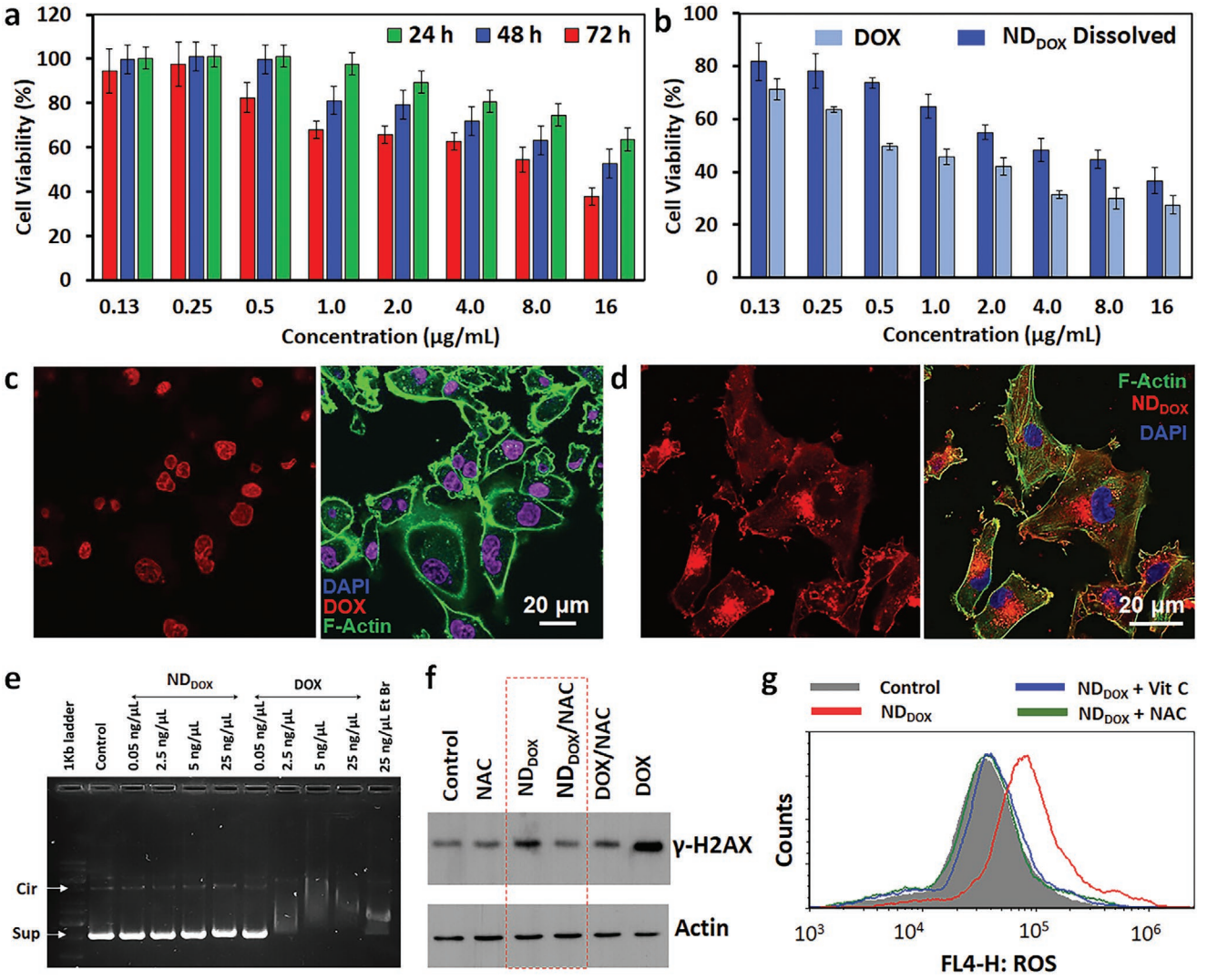

Figure 2. ROS-mediated cytotoxicity of ND$_{DOX}$. a) Cytotoxicity of ND$_{DOX}$ in MDA-MB-231 cells after 24, 48, and 72 h incubation at different concentrations. b) Cytotoxicity in MDA-MB-231 cells of free DOX and dissolved ND$_{DOX}$ after 48 h incubation. The data are shown as the mean ± standard deviation (SD) ($n = 3$). c,d) Representative confocal microscopy images of MDA-MB-231 cells treated with DOX (24 h, 0.5 μg mL^{-1}) (c) and ND$_{DOX}$ (24 h, 3 μg mL^{-1}) (d). The red signal arises from DOX (c) and ND$_{DOX}$ (d), whereas the green and blue signals represent F-actin and the nucleus in both panels. e) Gel migration assay showing the interaction of dissolved ND$_{DOX}$ and DOX with DNA plasmids (circular (Cir) and supercoiled (Sup)). f) DOX and ND$_{DOX}$-induced expression of γ-H2AX in MDA-MB-231 cells after 24 h incubation at concentrations corresponding to 2 × IC$_{50}$ at 72 h, analyzed in the presence and absence of a ROS scavenger (100×10^{-6} M, *N*-acetylcysteine, NAC). g) Flow cytometry assay showing ROS generation in MDA-MB-231 cells treated with ND$_{DOX}$ in the presence or absence of radical scavengers.

DNA damage is likely not a mechanism of the anticancer effects displayed by ND$_{DOX}$.

To gain a better insight into the mechanism by which ND$_{DOX}$ kills MDA-MB-231 cells, we analyzed the expression of γ-H2AX protein, which is commonly used as a specific protein marker of DNA damage. The levels of protein (γ-H2AX) were probed in the presence or absence of ROS scavenger *N*-acetylcysteine (NAC) (Figure 2f). The findings reveal that both DOX and ND$_{DOX}$ induced DNA damage, as confirmed by the increase in γ-H2AX levels (Figure 2f and Figure S6, Supporting Information). Moreover, after treatment with NAC the extent of DNA damage induced by ND$_{DOX}$ was completely reduced at the levels of untreated cells. This effect was not observed in cells exposed to DOX/NAC, which still exhibited DNA damage (Figure 2f and Figure S6, Supporting Information).

These results suggest that DNA damage induced by ND$_{DOX}$ in MDA-MB-231 cells is likely mediated by ROS generation. Hence, flow cytometry was used to directly assess the ability of ND$_{DOX}$ to produce ROS in the presence or absence of NAC or vitamin C as radical scavengers. As observed in Figure 2g, the ROS level in the treated MDA-MB-231 cells was higher than that in the untreated cells and the production of ROS was counteracted by treatment with vitamin C or NAC. Overall, these results indicate that the internalized ND$_{DOX}$ exert ROS-mediated cytotoxicity on cancer cells, including drug-resistant cell lines.

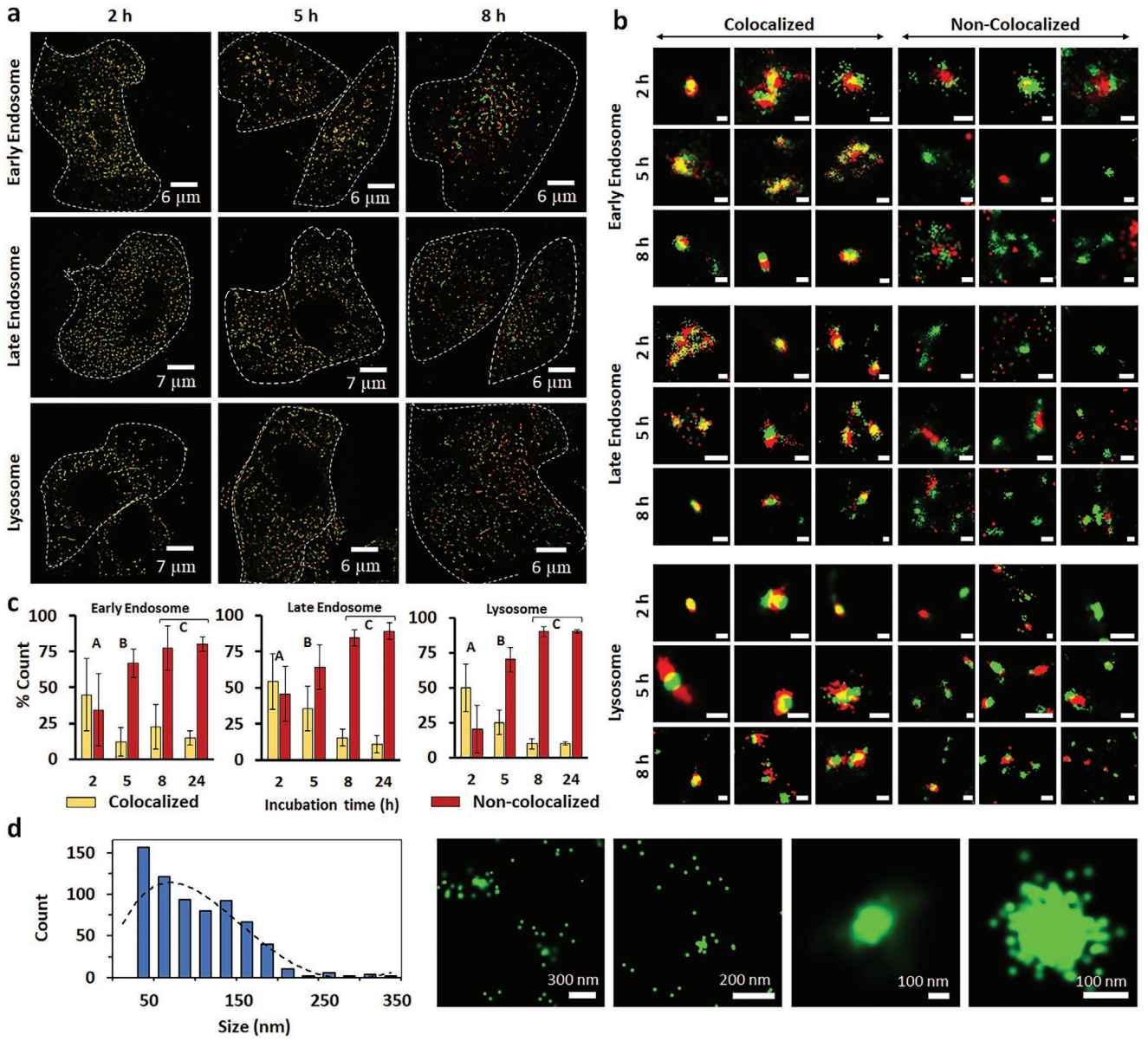

Figure 3. Intracellular trafficking and disassembly of ND_{DOX} in MDA-MB-231 cells analyzed by super-resolution microscopy. a) Representative multicolor STORM images of the MDA-MB-231 cells exposed for 2, 5, or 8 h to ND_{DOX} (green signal) and stained for early endosomes, late endosomes, and lysosomes (red signal). Experiments were repeated three times independently. b) Representative high-magnification images of the intracellular ND_{DOX} (scale bars = 200 nm). The red signal represents the intracellular vesicles, and the green signal represents ND_{DOX}. MDA-MB-231 cells were treated with ND_{DOX} at different incubation times (2–24 h). Cells were exposed to dual-labeled ND_{DOX} (activator reporter pair of AF 488/AF 647-Green) for 2 h. The culture medium was then replaced and the incubation was prolonged for 3, 6, and 22 h, corresponding to a total incubation time of 5, 8, and 24 h, respectively. The cells were fixed after 2, 5, 8, and 24 h incubation. The early endosomes, late endosomes, and lysosome vesicles were labeled for early endosome antigen 1, Rab 7, and lysosomal-associated membrane protein 1, respectively, and subsequently with the dual-labeled secondary antibody AF 555/AF 647-Red. c) Statistical analysis of ND_{DOX} colocalized and noncolocalized with early endosomes, late endosomes, and lysosomes as a function of incubation time. The data are shown as the mean ± SD ($n = 3$). At each time point, $n = 10$–12 cells, $n = 200$ nano-objects/cell were analyzed. The significantly different values ($p < 0.05$) between the bars are denoted by grouping into different letters. Statistical significance was determined using one-way ANOVA with 95% confidence interval and Tukey's multiple comparison. d) Size distributions and STORM images of nanoaggregates acquired after 24 h incubation. At each time point, $n = 10$ cells, $n = 200$–300 nano-objects/cell were analyzed.

2.3. Intracellular Trafficking, Disassembly, and Subcellular Localization of ND_{DOX}

To investigate the kinetics of cellular uptake, intracellular trafficking, and subcellular localization of ND_{DOX}, flow cytometry and super-resolution imaging studies were performed. Flow cytometry analysis showed a significant association of ND_{DOX} with MDA-MB-231 cells after 2 h of incubation (Figure S7, Supporting Information). Multicolor STORM images (**Figure 3**a and Figure S8, Supporting Information) of MDA-MB-231 cells

treated with ND_{DOX} at different incubation times and stained for lysosomes, early and late endosomes were analyzed. For STORM imaging, ND_{DOX} and the secondary antibody were dual-labeled using Alexa 488 *N*-hydroxysuccinimide (NHS) ester and Alexa 647 NHS ester (ND_{DOX} inner core and surface OH groups can react with NHS) and Alexa 555 NHS ester and Alexa 647 NHS ester, respectively. A representative gallery of analyzed ND_{DOX} and vesicles is shown in Figure 3b. By super-resolution microscopy analysis, we found ND_{DOX} colocalized (yellow signal or red signal in the proximity of green signal Figure 3b and Figure S8, Supporting Information) with endosomes and lysosomes, as well as noncolocalized ND_{DOX} (distinct green signal), indicating that ND_{DOX} can escape endo/lysosomes and access the cytosol. The statistical analysis of the STORM images obtained at different incubation times is shown in Figure 3c.

Specifically, after 2 h exposure, ND_{DOX} were colocalized with early/late endosomes and lysosomes. A significant decrease in colocalization with the early endosomes to 15% and late endo/lysosome to ≈ 30% was observed after 5 h incubation. Following 8 h incubation, limited colocalization was observed with all the compartments suggesting the endosomal escape of ND_{DOX}. Overall, these results indicate that the endocytic trafficking of ND_{DOX} occurs through early, late endosomes and lysosome and then the release to the cytosol occurred during the first 5 h of incubation. We postulate that the endosomal escape of ND_{DOX} is likely mediated by the proton sponge effect as ND_{DOX} exhibit slight buffering capacity between pH range of 5.6–6.7 (Figure S9, Supporting Information).[9] In addition, ND_{DOX} can partially disassemble inside the vesicles to release hydrophobic drug molecules that can disrupt the vesicles membrane by intercalating into the lipid bilayer, thereby favoring ND_{DOX} cytosolic release. Interestingly, STORM imaging and size distribution analysis of ND_{DOX} localized in the cytosol show that, following the endo-lysosomal escape, ND_{DOX} can disassemble into smaller nanoaggregates (30–180 nm) and free molecules (Figure 3d). It is worth mentioning that the presence of nanostructures smaller than ≈20 nm cannot be detected due to the limitation of STORM resolution, hence it cannot be excluded.

We next investigated the possible interactions of ND_{DOX} with other organelles once the drug is released in the cytosol (24 h incubation). We stained MDA-MB-231 cells exposed to ND_{DOX} for 24 h with specific markers for given organelles (plasma membrane, mitochondria, lipid rafts, microtubule, Golgi apparatus, and endoplasmic reticulum, ER) and analyzed color scattered plots (Figure S10, Supporting Information) from confocal microscopy images. The analysis suggests negligible colocalization (assessed by Pearson correlation coefficient-PCC values) with microtubuli (**Figure 4**a1–3 and Figure S11, Supporting Information, PCC = 0.145) and Golgi complex (Figure 4b1–3 and Figure S11, Supporting Information, PCC = 0.125). Conversely, significant colocalization of ND_{DOX} with the ER (Figure 4c1–3 and Figure S11, Supporting Information, PCC = 0.580), plasma membrane (Figure 4d1–3 and Figure S11, Supporting Information, PCC = 0.345), and mitochondria (Figure 4e1–3 and Figure S12, Supporting Information, PCC = 0.563) was observed. Interestingly, in treated cells, mitochondria were found localized in the perinuclear region (Figure 4e2 and Figure S12, Supporting Information), a phenomenon which was not observed in untreated cells (Figure S13, Supporting Information).

Moreover, single-molecule super-resolution imaging of MDA-MB-231 cells, treated with ND_{DOX}, revealed the nanoaggregates colocalized with tubular mitochondrial nanostructures (Figure 4g1–6). The preferential compartmentalization of the species in the plasma membrane, ER, and mitochondria in cancer cells was ascribed to their selective affinity for the membrane lipid raft domains via hydrophobic interactions. Lipid rafts are membrane microdomains enriched in cholesterol and sphingolipids. Given that high levels of cholesterol in the mitochondrial membrane have been reported in cancer cells,[21] we examined the distribution of lipid rafts domains in tumor cells and their possible interaction with ND_{DOX} by staining the treated cells with the lipid raft marker cholera toxin-B. In the untreated MDA-MB-231 cells, lipid rafts were mostly located at the plasma membrane and inside the cells (Figure S14, Supporting Information). In contrast, in cells treated with ND_{DOX} (Figure 4f3 and Figure S15, Supporting Information), lipid rafts were localized in the perinuclear region and colocalized with ND_{DOX} nanoaggregates and/or released drug molecules (PCC = 0.524). The lipid raft marker was also found colocalized with mitochondria (Figure S16, Supporting Information). These findings indicate that mitochondrial raft domains are preferential binding sites for ND_{DOX} nanoaggregates or released drug molecules. Previous studies performed with the synthetic phospholipid drug edelfosine[22] have shown that the accumulation of the drug in the mitochondria of tumor cells is mediated by lipid rafts. In this context, the physical interaction between ER and mitochondria[23] could explain the colocalization of ND_{DOX} with both these organelles.

Our study reveals that ND_{DOX} are rapidly taken up by endocytosis and trafficked through the endo-lysosomal pathway to the cytosol within 5 h of incubation. ND_{DOX} disassemble to release drug molecules that are sequestrated and immobilized through lipid raft domains in the mitochondrial and ER compartments as well as in the plasma membrane. The overall intracellular trafficking and our hypothesis for the mode of action of ND_{DOX} are depicted in Figure 4h.

The mitochondria compartmentalization of ND_{DOX} nanoaggregates or released drug molecules can explain the production of ROS in cancer cells via redox cycling of quinone moieties[24] as shown in Figure 4h. Drug molecules bear a quinone that can promptly react with the dihydronicotinamide-adenine dinucleotide phosphate (NADPH) to form semiquinone that is then oxidized by oxygen to generate superoxide anion $O_2^{\cdot -}$ and other ROS species, leading to DNA damage and cell death.[17,25] The observed translocation of the mitochondria in the perinuclear region may increase the likelihood of cellular oxidative stress by enhancing ROS concentration nearby the cell nucleus. Furthermore, the preferential tropism for mitochondria of ND_{DOX} is likely correlated to their capability to overcome drug resistance in cancer cells. The consumption of NADPH by ND_{DOX} for ROS production limits the adenosine triphosphate synthesis, which is important for the efflux pump function.

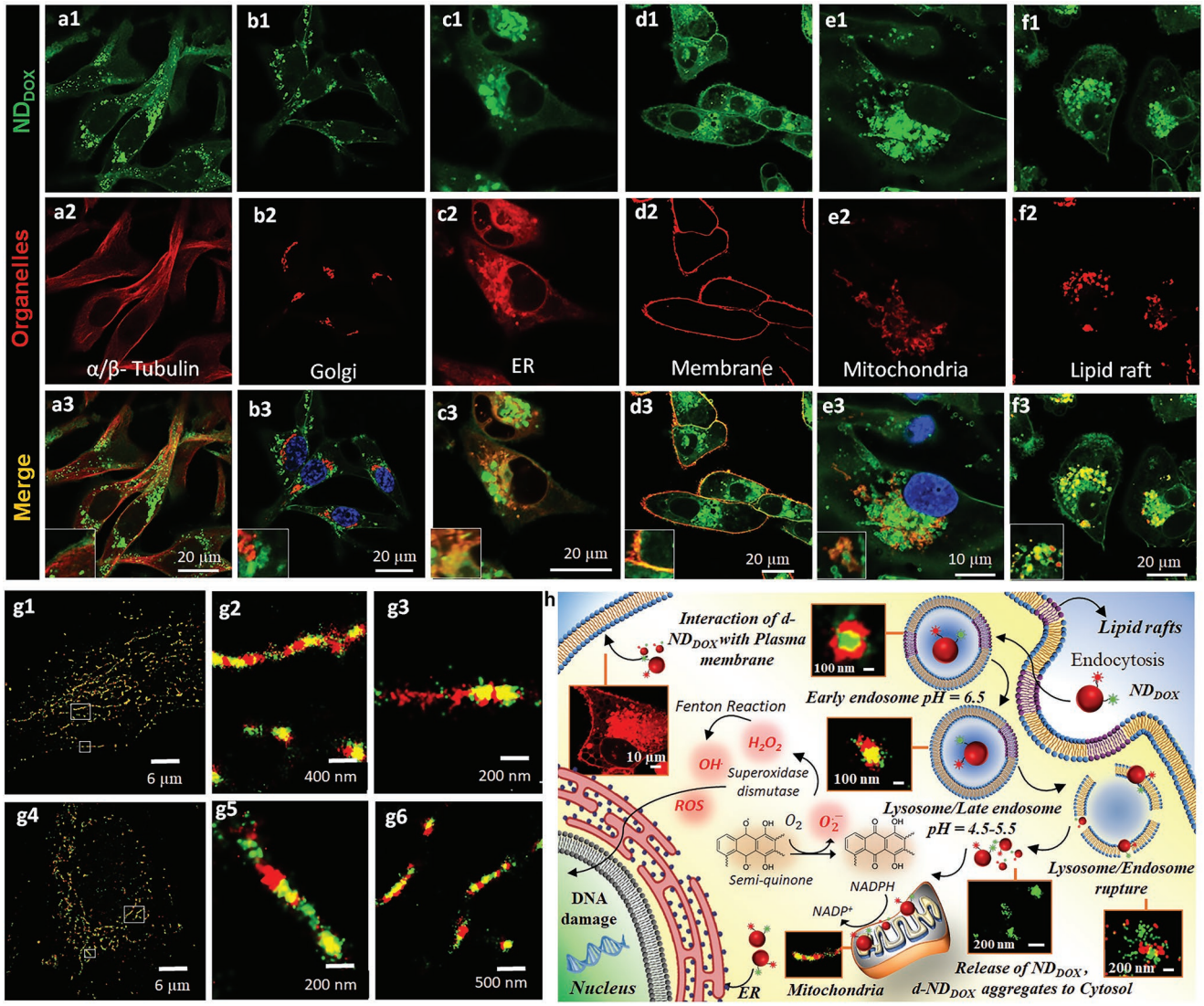

Figure 4. Subcellular compartmentalization of ND_{DOX} in the mitochondria of MDA-MB-231 cells. a–f) Representative confocal microscopy images of MDA-MB-231 cells incubated with ND_{DOX} (green) for 24 h and stained for different organelles (red): α/β tubulin (a1–a3), Golgi (GM130, b1–b3), ER (ER-Tracker (tm) Green (BODIPY FL Glibenclamide, c1–c3), cellular membrane (wheat germ agglutinin, d1–d3), mitochondria (TOM20, e1–e3), and lipid rafts (cholera toxin, f1–f3). Insets in (a3)–(f3) show magnified details of the respective main images. g) Multicolor STORM images of MDA-MB-231 cells showing the interaction between mitochondrial tubular nanostructures (TOM20-red) and ND_{DOX} (green) after 24 h incubation. g1,g4) Large view of representative cells. g2,g3,g5,g6) Magnified images of the square sections in (g1) and (g4), respectively (for images shown in (a)–(g), $n > 20$ images from three independent experiments). h) Scheme showing the intracellular trafficking, endosomal escape, disassembly, mitochondrial sequestration, and mechanism of cell death by ND_{DOX}.

2.4. Selective Cytotoxicity of ND_{DOX} toward Cancer Cells in 3D Static and Dynamic Cell Coculture Systems

To assess the impact of ND_{DOX} on healthy cells and their potential to selectively target cancer cells, we first studied their cytotoxic effect in 3T3 healthy fibroblasts. Unlike DOX, which accumulated in the nucleus (Figure S17a, Supporting Information), ND_{DOX} particles were predominantly retained in cell fibroblast cytoplasm (Figure S17b, Supporting Information) even after a longer exposure time (96 h incubation). This might explain why ND_{DOX} displayed negligible toxicity toward fibroblasts, as compared to DOX, which was toxic at low doses (**Figure 5**a,b). To explain this, we quantified the presence of lipid rafts in 3T3 cells. Compared to cancer cells, lipid rafts in 3T3 cells were less abundant, and consistently the extent of colocalization of ND_{DOX} with both lipid rafts (Figure S18, Supporting Information, PCC = 0.258) and mitochondria (Figure 5c and Figures S19 and S20, Supporting Information, PCC = 0.210) was limited. In addition, the mitochondria appeared evenly distributed throughout the treated 3T3 cells. These results suggest that the low affinity of ND_{DOX} for the mitochondria in healthy cells is correlated to their reduced cytotoxicity. Of note, the intracellular accumulation of ND_{DOX} in fibroblasts, even at high concentrations and prolonged incubation time (96 h), did not exert any detrimental effects on cell morphology and viability.

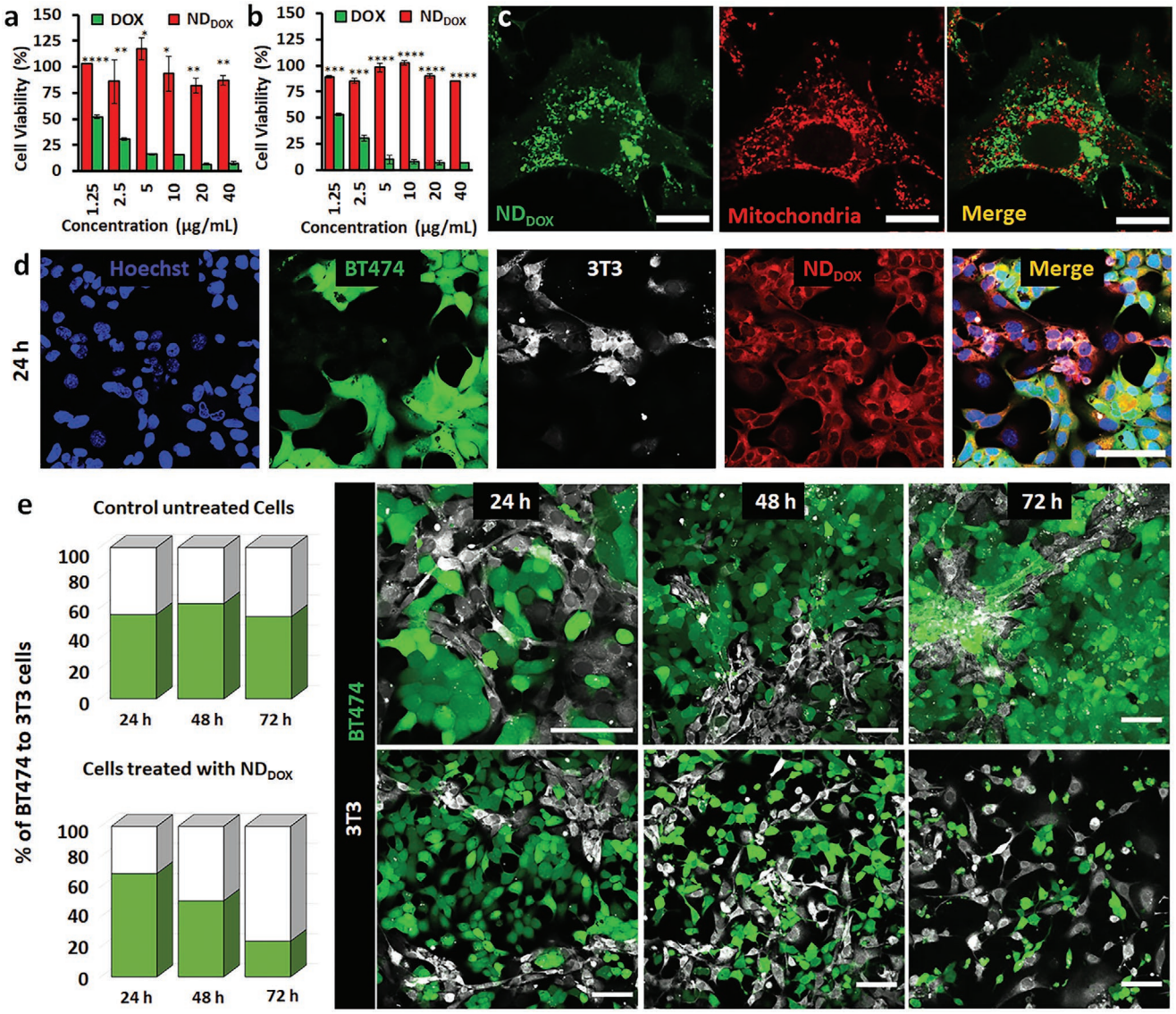

Figure 5. Selective toxicity of ND_{DOX} in 2D coculture of 3T3 fibroblast and BT474 breast cancer cells. a,b) DOX and ND_{DOX} cytotoxic effect on 3T3 fibroblasts after 72 h (a) and 96 h (b) exposure. Data are shown as the mean ± SD ($n = 3$). **** p-value ≤ 0.0001, *** p-value ≤ 0.001, ** p-value ≤ 0.01, * p-value ≤ 0.05 as calculated using one-way ANOVA with 95% confidence interval and Tukey's pairwise comparison. c) Confocal microscopy images of the 3T3 fibroblasts treated with 5 μg mL^{-1} ND_{DOX} (green) for 24 h and stained for mitochondria (TOM20, red). Scale bars are 20 μm ($n = 20$ images two independent experiments). d) Confocal microscopy images of a coculture of BT474 breast cancer cells (green, stained with CellTracker Green CMFDA Dye) and 3T3 fibroblasts (white, stained with CellTracker Deep Red dye) showing the uptake of ND_{DOX} (red, 25 μg mL^{-1}) after 24 h. Cell nuclei were stained with Hoechst (blue). e) Graphical representation and confocal microscopy representative images of the cocultured BT474 breast cancer cells (green, stained with CellTracker Green CMFDA Dye) and 3T3 fibroblasts (white, stained with CellTracker Deep Red dye) treated in the absence (control untreated cells) or in the presence of 25 μg mL^{-1} ND_{DOX} for 24, 48, or 72 h. Scale bars are 50 μm in all images ($n = 3$ independent experiments).

Next, we sought to confirm the selective cytotoxicity of ND_{DOX} toward cancer cells in 2D cocultures of BT474 breast cancer cells (green) and 3T3 (white) fibroblasts. Although ND_{DOX} were equally internalized by both cell lines (Figure 5d), they predominantly caused cell death in BT474 (Figure 5e and Figure S21 and S22, Supporting Information). In fact, image analysis and quantification of the cancer cell-to-fibroblast ratio (Figure 5e and Figure S22, Supporting Information) revealed a significant decrease in the number of cancer cells over time due to cell death and detachment.

Furthermore, we prepared 3D tumor microtissues by coculturing BT474 and 3T3 cells on a collagen scaffold in U-Cup perfusion bioreactor device and studied the ability of ND_{DOX} to accumulate in such a complex tumor model (**Figure 6**a). Perfusion-based cell cultures in bioreactors have demonstrated the ability to mimic human tissue constructs with comparable biological and structural characteristics.[26,27] In particular U-Cup perfusion bioreactors have been bioengineered to test anticancer drugs and nanodrugs in colorectal cancer and human breast cancer cell lines with the cultured tumor cells efficiently

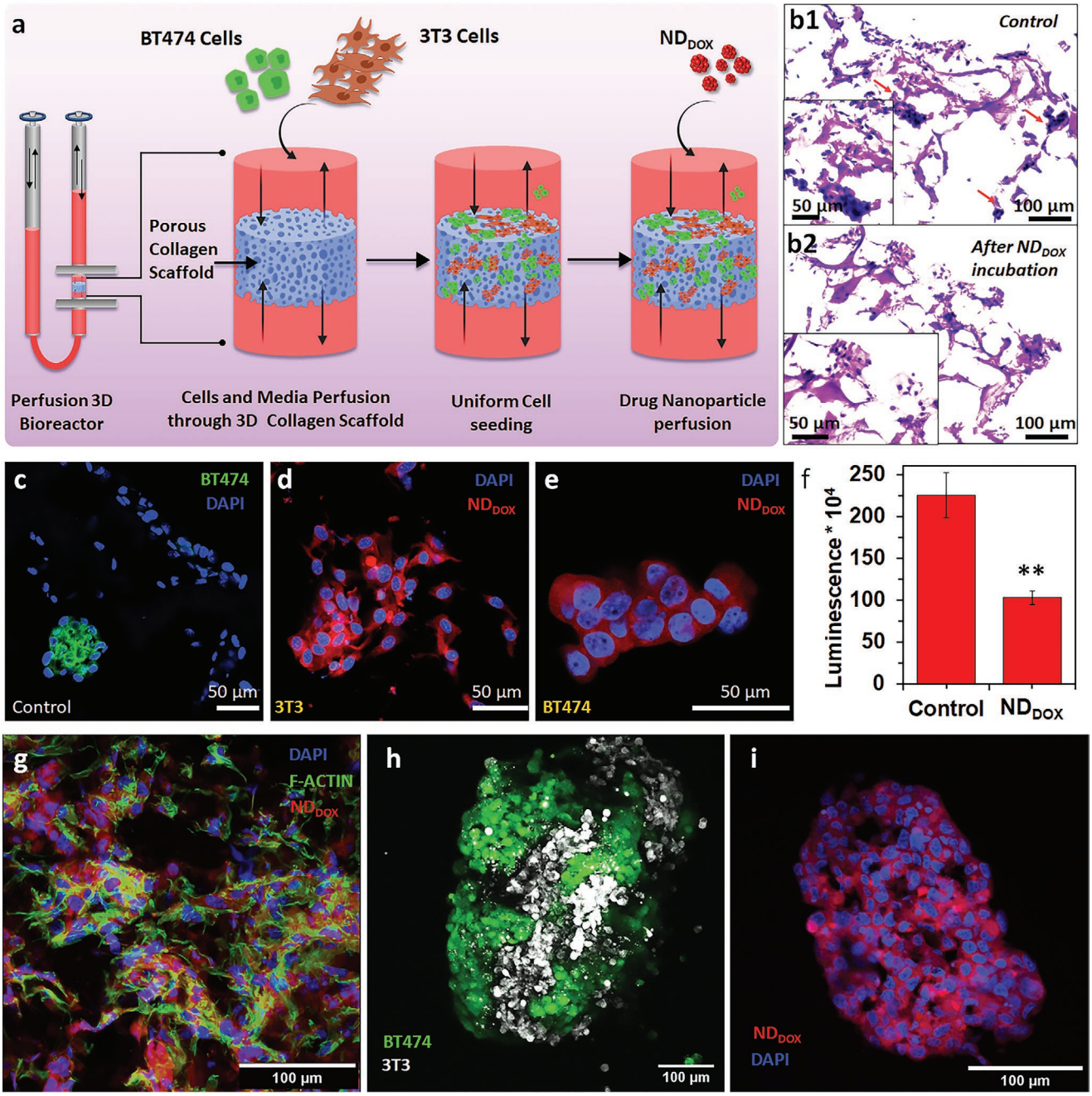

Figure 6. Toxicity and uptake of ND_{DOX} in static and perfusion 3D coculture of 3T3 fibroblast and BT474 cancer cells. a) Schematic showing the 3D cocell culture in U-Cup Bioreactor with collagen scaffold. b) H&E staining of the sections of collagen scaffold cocultured with 3T3 and BT474 cells before (b1) and after (b2) incubation with ND_{DOX}. The red arrows point to BT474 cells. c) Representative confocal microscopy image of a section from the collagen scaffold cocultured with 3T3 and BT474 cells before incubation with ND_{DOX}. Nuclei are stained with DAPI and BT474 breast cancer cells are stained in green with CellTracker Green CMFDA Dye. Scale bar = 50 µm. d,e) Magnified confocal microscopy of 3T3 cells (d) and BT474 cells (e), respectively, from 3D perfusion collagen scaffold cocultured with 3T3 and BT474 cells showing uptake of ND_{DOX} (red) by both the cell types when treated with 10 µg mL^{-1} ND_{DOX}. Scale bar = 50 µm. f) Luminescence representing the cell viability in collagen scaffold cocultured with 3T3 and BT474 cells before and after incubation with 10 µg mL^{-1} ND_{DOX} for 24 h measured using CellTiter-Glo 3D cell viability kit. Data are shown as the mean ± SD (n = 3). ** p-value ≤ 0.01. g) Confocal microscopy representative image of collagen scaffold cocultured with 3T3 and BT474 cells stained for F-actin (phalloidin—green) and nucleus (DAPI—blue) after incubation with 10 µg mL^{-1} ND_{DOX} (red) for 24 h. Scale bar = 100 µm. h,i) Confocal microscopy images of 3D spheroids composed of cocultured BT474 breast cancer cells (green, stained with CellTracker Green CMFDA Dye) and 3T3 fibroblasts (white, stained with CellTracker Deep Red dye) (h), and after treatment with 25 µg mL^{-1} ND_{DOX} (red) for 72 h (i).

mimicking some of the functional features observed "in vivo".[27,28]

BT474 and 3T3 cells were cocultured in 1:1 ratio onto a collagen scaffold for up to 7 days within U-cup perfusion flow bioreactor. Continuous medium flow was established from day 4 on in the case of dynamic cocultures (Figure 6a) and the cocultures were then treated with ND_{DOX} for 24 h. Before and after the treatment with ND_{DOX}, cell distributions within the scaffold and ND_{DOX} uptake were monitored by Hematoxylin and Eosin (H&E) staining and confocal microscopy, respectively.

Figure 6b1,c and Figure S23 in the Supporting Information confirmed the presence of both BT474 and 3T3 cells in the 3D coculture. The BT474 cells can be distinguished due to their cluster appearance as indicated by red arrows and from confocal microscopy by staining with CellTracker Green 5-chloromethylfluorescein diacetate (CMFDA) dye (Figure 6c and Figure S23b-green, Supporting Information). Figure 6b2 and Figure S24a,b in the Supporting Information show the different sections of collagen scaffold after H&E and 4′,6-diamidino-2-phenylindole (DAPI) staining when treated with the ND_{DOX} for 24 h. Numerous (n = 52) scaffold sections from the perfused 3D coculture were analyzed to verify the ability of ND_{DOX} to penetrate the tissue-like structure. Figure 6d,e,g and Figure S24c in the Supporting Information shows that ND_{DOX} were able to diffuse throughout the scaffold into the extracellular matrix and the whole cellular mass. In addition, ND_{DOX} were successfully uptaken by BT474 and 3T3 cells (Figure 6g) with no signs of nuclear accumulation. Interestingly, the analysis of scaffold sections showed negligible amount of BT474 cells after the drug treatment which was also confirmed by flow cytometry (Figure S24d, Supporting Information), while cell proliferation was reduced by more than ≈ 50%, as assessed by the 3D cell viability assay which can be assigned to toxicity of ND_{DOX} toward BT474 cells (Figure 6f).

Overall, these results indicated that ND_{DOX} traverse the extracellular matrix, penetrate through tumor microtissues and are effectively internalized by cancer cells. To further verify the ability of ND_{DOX} to penetrate 3D multicellular tissue like systems, 3D spheroids containing BT474 breast cancer cells (green) and 3T3 fibroblasts (white) were prepared using the hanging drop methodology (Figure 6h) and were treated with 25 μg mL^{-1} ND_{DOX} particles. Seventy-two hours after the administration, ND_{DOX} could permeate the whole spheroid cellular mass and reach the cells located at the core of the spheroid, where they accumulate in the cytoplasm, as demonstrated by serial sectioning (Figure 6i).

We postulate that the selective ROS-mediated cytotoxicity of ND_{DOX} toward cancer cells can be ascribed to the selective binding of the drug to mitochondrial lipid raft domains in cancer cells. Cancer cells are known to produce and consume more ROS than healthy cells.[24,29] While a moderate amount of ROS is required for maintaining diverse cell functions, transformed tumor cells use an augmented ROS signaling to drive proliferation and other events related to tumor progression.[30,31] Given the high basal level of ROS found in neoplastic cells, these cells are more vulnerable than healthy cells to sustained increases in oxidant stress, which results in cell death.[30,32] Mitochondria-targeted anticancer drugs have been developed to overcome drug resistance and reduce side effects in healthy cells.[33–35] These compounds are chemically modified with lipophilic triphenylphosphonium cations, which localize the drugs into the mitochondria via their positive charges and hydrophobic surface.[35] The positive charges of the lipophilic cations allow them to enter the negatively charged inner mitochondrial membrane. However, the major hurdles of these approaches are the low accumulation of drugs in the mitochondria, poor selectivity of drugs for cancer over healthy cells as well as the need for photodynamic therapy for ROS generation.[33]

Unlike other literature-reported systems,[33–35] ND_{DOX} are negatively charged amphiphilic species that preferentially accumulate in the mitochondria of cancer cells via hydrophobic interactions with lipid raft domains. Therefore, the redox activity of ND_{DOX} can ensure a sustained production of cytotoxic ROS in the mitochondria.

2.5. ND_{DOX} Display Limited Toxicity against Cardiomyocytes

Next, we investigated the possibility that ND_{DOX} might be less toxic for cardiac cells than DOX, which is known to cause cardiomyopathy.[19,36] Induced pluripotent stem cell (iPSC)-derived cardiomyocytes (CMs) were treated with DOX revealing that the drug accumulates in the cell nuclei even at very low doses and induces high levels of cell death (**Figure 7**a–c and Figure S25, Supporting Information). As previously stated, DOX nuclear accumulation is responsible for the activation of the DNA damage response pathway.[25]

On the contrary, when the CMs were exposed for up to 72 h to high doses of ND_{DOX}, we observed a very limited toxicity. In addition, ND_{DOX} did not show any nuclear localization (Figure 7d,e and Figure S26, Supporting Information) and accumulated in CMs cytosolic compartment. More importantly, CMs treated with ND_{DOX} kept contracting even when exposed for 72 h at the highest concentration of ND_{DOX} studied (25 μg mL^{-1}) (Videos S3–S6, Supporting Information). As a comparison, CMs treated with 6–25 μg mL^{-1} DOX stopped beating after 48 h, indicating loss of cell functioning and cell death (Videos S7–S9, Supporting Information). Color scattered plot and confocal images (Figure 7e and Figures S27 and S28, Supporting Information) show partial colocalization between the mitochondria (red) and ND_{DOX} (green) in CMs, even at a high dose of ND_{DOX} (12.5 μg mL^{-1}). This finding is consistent with that observed in 3T3 fibroblasts and indicates that the internalized ND_{DOX} do not preferentially interact with cardiomyocytes mitochondria, as is—instead—the case in cancer cells (Figure S28, Supporting Information). Moreover, flow cytometry data (Figure 7f) and confocal microscopy analysis (Figure 7g and Figure S29, Supporting Information) indicate no increase in ROS production in contractile CMs treated with ND_{DOX} compared to untreated control cells. Overall, these results suggest that ND_{DOX} did not exert a cytotoxic effect on cardiomyocytes or fibroblasts because of its inability to accumulate in the cell nucleus.

2.6. In Vivo Biosafety and Biodistribution of Indium-111-Labeled ND_{DOX}

To assess biosatefy, three female mice C57/BL6J were intravenously injected with ND_{DOX} (2 mg ND_{DOX} kg^{-1}). The animals

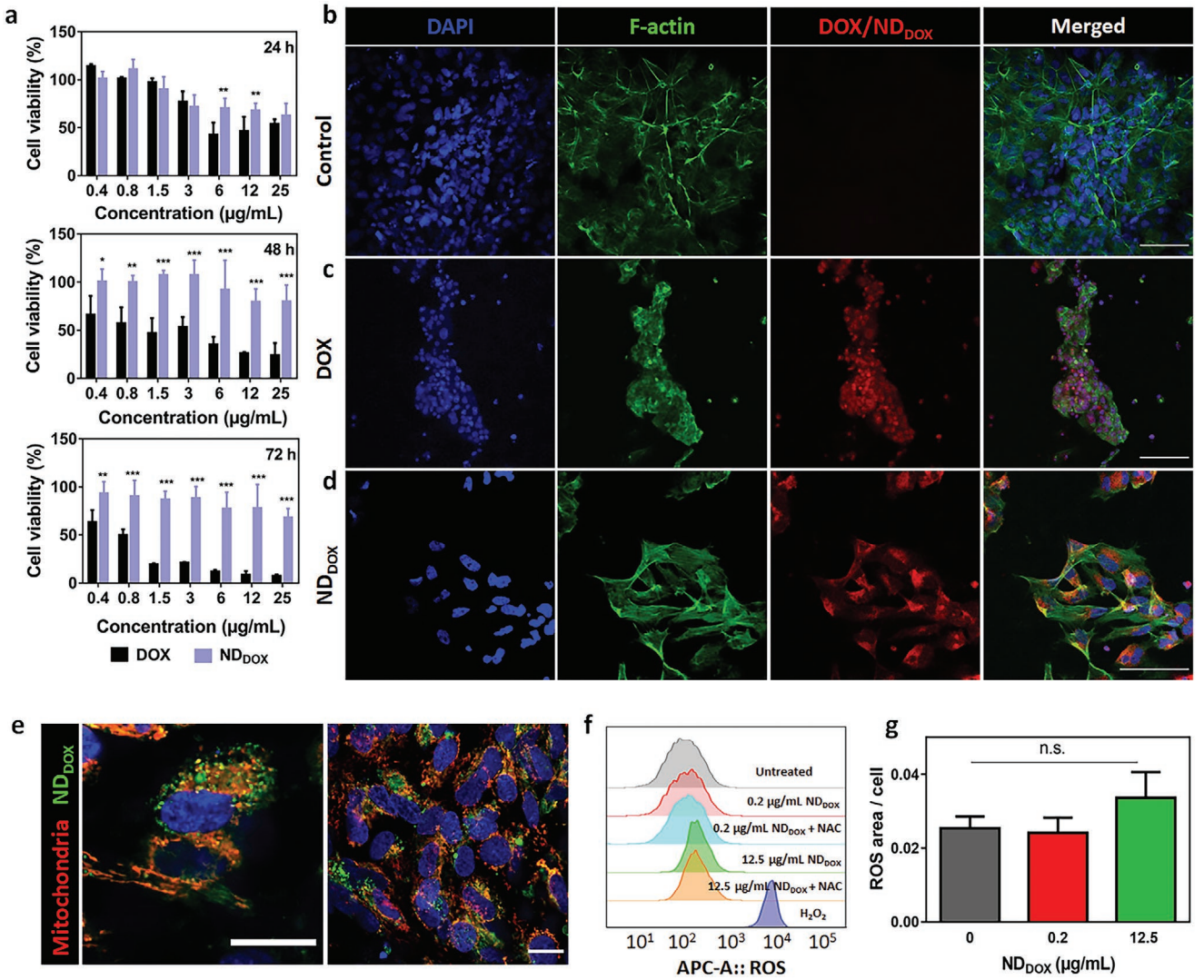

Figure 7. ND_{DOX} are not cardiotoxic and do not induce ROS production in iPSC-derived cardiomyocytes. a) iPSC-derived cardiomyocytes viability after treatment with DOX and ND_{DOX} was measured by PrestoBlue. The percentage of live cells normalized to the control untreated cells is reported for each time point (24, 48, and 72 h; mean ± SD, $n = 4$). *** p-value < 0.001, ** p-value < 0.01, * p-value < 0.05 (two-way ANOVA followed by Bonferroni post-test). b–d) Representative confocal microscopy images of untreated cardiomyocytes (b), cardiomyocytes treated with DOX (c) and cardiomyocytes treated with ND_{DOX} (d). Nuclei are stained with DAPI in blue, F-actin in green and DOX/ND_{DOX} in red. e) iPSC-derived cardiomyocytes after 5 h treatment with ND_{DOX} (green signal) stained with mitotracker deep red (red signal). Colocalization is visible from the yellow areas. Scale bars: 20 µm. f) Flow cytometry analysis of ROS production in untreated iPSC-derived cardiomyocytes, CMs treated with 0.2 µg mL^{-1} ND_{DOX} in the absence or presence of NAC scavenger, CMs treated with 12.5 µg mL^{-1} ND_{DOX} in the absence or presence of NAC scavenger, and cells treated with H_2O_2. Representative flow cytometry plots of $n = 3$ independent experiments. g) Ratio of ROS area to cell number determined from confocal microscopy images (acquired at 20× magnification) of the same cell samples used for the cytometry studies represented in (f)) (see Figure S29, Supporting Information). Data are shown as the mean ± SD ($n = 3$). No significant differences were found using one-way ANOVA followed by Tukey's multiple comparison test (n.s., nonsignificant).

were monitored for their activity and physical conditions over 10 d (Table S2, Supporting Information). The recorded data show a survival rate of 100% for the treated mice, without signs of stress or suffering. Furthermore, no significant differences in the weight of the animals were observed 10 days post-ND_{DOX} administration. These results suggest that ND_{DOX} can be safely used for further in vivo experiments.

Next, ND_{DOX} particles were successfully radiolabeled with the short-lived and single photon γ-emitting isotope of indium-111 (^{111}In), as shown by chromatography data (Figures S30 and S31, Supporting Information). The purified labeled ND_{DOX} showed excellent radiochemical stability (>99.9%) up to 24 h post-labeling at all tested temperatures. A slight reduction in radiochemical stability to >80% after incubation in saline solution and biological media (Plasma Lyte) was observed (Figure S32, Supporting Information). The radioactivity of ND_{DOX} activity significantly decreased when the antagonist ethylenediaminetetraacetic acid chelator was used. Overall, these results provide evidence for adequate radiolabeling capacity and stability of the tested

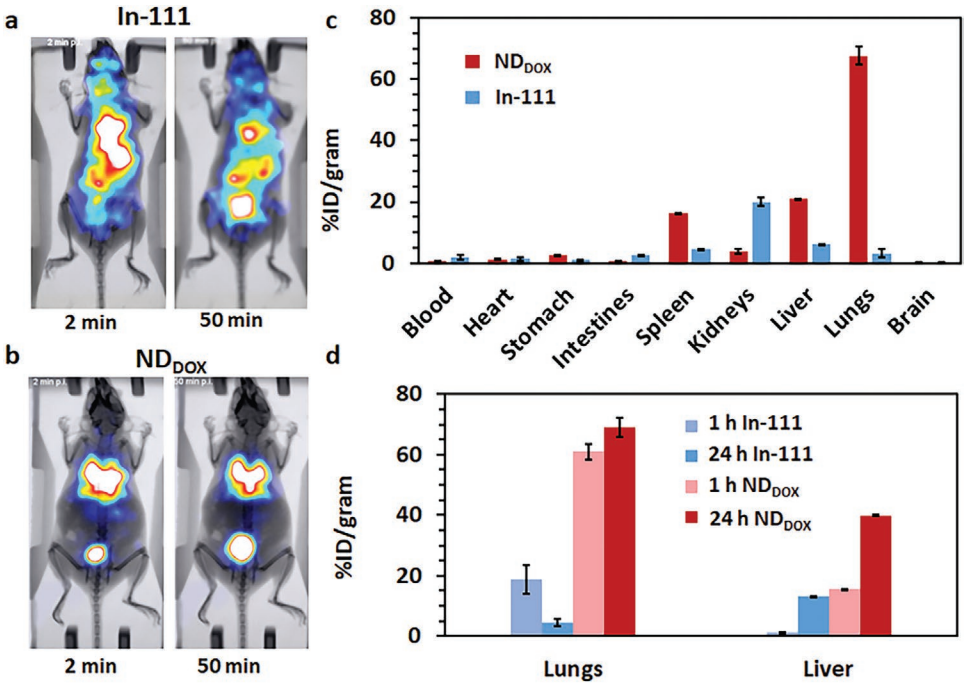

Figure 8. In vivo biodistribution of In-111 and 111In-labeled ND_{DOX}. a,b) Representative single photon emission computed tomography (SPECT) images of control mice, injected with just the ligand (In-111) (a), and mice injected with ^{111}In-labeled ND_{DOX} (b) showing the biodistribution just after injection and 50 min p.i. Imaging was performed with γ-eye BIOEMTECH, with a frame rate of 2 min, on dynamic mode ($N = 2$). c) % ID g^{-1} for both control and experimental mice, based on ex vivo biodistribution measurements. d) % ID g^{-1} in lungs and liver 1 h versus 24 h post-injection in In-111- and ND_{DOX}-treated mice.

nanoparticles, rendering them appropriate candidates for all tested procedures.

For the in vivo biodistribution studies, the ^{111}In-labeled ND_{DOX} and free In-111, used as control, were injected to C57/BL6J female mice and the biodistribution was investigated with γ-eye BIOEMTECH, at different time points (**Figure 8**a, Figure S33, Supporting Information, Figure 8b, and Figure S34, Supporting Information). The imaging results revealed a high accumulation of ND_{DOX} in lungs and bladder (Figure 8b). The signal arising from bladder can be assigned to the loosely bound In-111 as this accumulation is also visible in the control mice 50 min post-injection (Figure 8a). After 24 h the mice were sacrificed and the percentage of injected dose per gram of organ (% ID g^{-1}) of various organs was measured (Figure 8c). It was found that the free In-111 was primarily present in kidneys (≈20%), with trace amounts in liver, lung and spleen (≈5% in each organ). On the contrary, the ND_{DOX} predominately localize in the lungs (≈60%), followed by the liver and the spleen (≈20%). While a significant reduction in % ID g^{-1} was observed after 24 h for the free In-111 (Figure 8d), there was an increase in % ID g^{-1} for different organs, from 1 to 24 h post-injection of ND_{DOX}, suggesting a prolonged circulation of ND_{DOX} in the blood. The mechanism of lung accumulation of ND_{DOX} is currently under investigation; however, it might be related to the hydrophobicity and tendency of the nanodrug to interact with lipids. It is reported that hydrophobic drugs with molecular weight above >300 Da can associate with lipids in the lungs being retained there for long time.[37]

Finally, to directly verify the ability of ND_{DOX} to remain available in the blood upon interaction with immune cells, ex vivo human immune cells derived from buffy coat were incubated with ND_{DOX} up to 96 h. Flow cytometry data (Figure S35a, Supporting Information) suggest an association of ND_{DOX} with immune cells, with a peak at 12 h with no further increase over time. Staining with calcein O,O′-diacetate tetrakis(acetoxymethyl) ester (calcein AM) confirms the viability of the immune cells after 96 h (Figure S35b, Supporting Information). In addition, the spectroscopic analysis of the remaining plasma supernatant, collected after removal of immune cells by centrifugation (Figure S35c, Supporting Information), indicates that the concentration of ND_{DOX} does not change significantly over time, suggesting a modest clearance by immune cells. Overall, these results indicate that, despite a modest sequestration of the nanoparticles by immune cells, ND_{DOX} likely remain available in the blood, for accumulation in tumors.

These preliminary ex vivo and in vivo results and the unexpected lung accumulation of ND_{DOX} pave the way for future studies on the application of ND_{DOX} nanodrug for the treatment of lung cancer.

3. Conclusion

A strategy for selectively killing cancer cells, with minimal impact on the viability of healthy cells, is reported. Transformed nanodrugs were obtained using a conventional anticancer drug and a simple and green ultrasound technology, in aqueous solutions, without resorting to any chemical reagents or organic solvents.

The nanodrugs were found stable in serum and maintained their antiproliferative activity against different types of cancer cells, including cells resistant to DOX. Importantly the nanodrugs penetrate tumor microtissues and kill cancer cells while imparting negligible toxicity toward healthy fibroblasts and cardiomyocytes. The strong interaction of nanodrugs with the lipid raft domains is likely to explain the preferential tropism of ND_{DOX} for the mitochondria of cancer cells. The confinement of the ND_{DOX} nanoaggregates in the mitochondria triggered the production of high levels of ROS, leading to DNA damage and cell death. The in vivo biodistribution of the nanodrug in healthy mice shows that the ND_{DOX} was predominately accumulated in the lungs. Overall, the present findings indicate ND_{DOX} as a promising candidate for in vivo studies on tumor models.

4. Experimental Section

Synthesis of ND_{DOX}: Sonication of a 10 mL solution containing 0.5 mg mL^{-1} DOX was performed in Milli-Q water for up to 4 h at an ultrasonic frequency and power of 490 kHz and 2 W cm^{-2}, respectively. The nanodrug particles were then separated by centrifugation at 5000 × *g* for 10 min and washed three times with Milli-Q water before characterization. The morphology of particles was examined using SEM, TEM, AFM, and STORM. The chemical composition of the dissolved ND_{DOX} was determined using mass spectrometry, NMR, and HPLC (see the Supporting Information for details).

ROS Detection: Intracellular ROS production was determined in MDA-MB-231 cells and iPSC-derived cardiomyocytes using Cellular Reactive Oxygen Species Detection Assay Kit following the manufacturer's protocol. Briefly, MDA-MB-231 cells (800 000) were plated into T-25 flasks for 24 h and then incubated for 24 h with 0.2 μg mL^{-1} ND_{DOX} in the presence or absence of 100 × 10^{-6} M NAC or vitamin C. Under low light conditions, a ROS-specific detection probe was added and incubated for 60 min at 37 °C. The cells were harvested, transferred to foil-wrapped tubes, and immediately analyzed by flow cytometry. For iPSC-derived cardiomyocytes, cells were differentiated in six-multiwell plates, and once the cardiomyocytes were beating, incubation with 0.2 μg mL^{-1} ND_{DOX} in the presence or absence of 100 × 10^{-6} M NAC followed. Under low-light conditions, an ROS-specific detection probe was added and incubated for 5 min at 37 °C. The cells were harvested and dissociated using the Multi Tissue Dissociation Kit 3, transferred to foil-wrapped tubes, and analyzed by flow cytometry. Nontreated cells stained with the ROS probe were used as a control. H_2O_2-treated iPSC cardiomyocytes were stained with ROS and used as a positive control for ROS production. The samples that were measured by flow cytometry were subsequently imaged by confocal microscopy.

ND_{DOX} Internalization and Subcellular Compartmentalization: MDA-MB-231 cells were incubated with DOX or ND_{DOX} and imaged on a Nikon A1R laser scanning confocal microscope for nanoparticles internalization analysis. For subcellular compartmentalization studies, MDA-MB-231 were treated with ND_{DOX} or DOX and at the designated time, the cells were washed with PBS, fixed, permeabilized, and blocked prior to immunofluorescence. The incubation with the respective primary antibodies was done for 2 h at room temperature or overnight at 4 °C, followed by secondary antibody incubation for 1 h at room temperature. For lipid raft staining, the cells were incubated with 5 μg mL^{-1} cholera toxin fluorescein isothiocyanate (FITC) conjugate for 1.5 h after fixation. For membrane staining, the cells were incubated with wheat germ agglutinin (WGA)–Alexa Fluor 488 conjugate for 20 min after fixation. Colocalization values were determined using the Pearson's correlation function with ImageJ software. Lipid rafts were imaged by cholera toxin-B FITC, which selectively binds to the ganglioside present in these domains. For ER staining, live-cell imaging was performed immediately after the addition of ER-Tracker(tm) Green (BODIPY FL Glibenclamide) to cells.

STORM: For STORM analysis, ND_{DOX} were dual-labeled using NHS ester Alexa Fluoro 488 and NHS ester Alexa 647. Specifically, both dyes were incubated with ND_{DOX} solution (1 mg mL^{-1} of sodium bicarbonate buffer pH = 9) and the solution was stirred for 2 h. After, the mixture was centrifuged (9000 g, 5 min) and the particles were washed with water three times before STORM imaging using Nikon N-STORM system equipped with a Nikon 100× 1.4 numerical aperture (NA) oil immersion objective. STORM images were processed and the population of nano-objects analyzed with the STORM module of the NIS Elements Nikon software. For intracellular trafficking, MDA-MB-231 cells were exposed to ND_{DOX} (5 μg mL^{-1}) for 2–24 h. The particles were retrieved after 2 h and kept at 37 °C for 5, 8, or 24 h in fresh media. At each timepoint, the cells were fixed, permeabilized, and blocked. The cells were then incubated with rabbit-early endosome antigen 1 (EEA-1) monoclonal antibody (2 μg mL^{-1}), rabbit-Rab7 monoclonal antibody (2 μg mL^{-1}), or rabbit lysosomal-associated membrane protein 1 (LAMP-1) (1 μg mL^{-1}) for 1.5 h, followed by washing three times with PBS and further incubation for 1 h with dual-labeled AF 555/647 goat antirabbit conjugate secondary antibody (2 μg mL^{-1}). Mitochondria staining was carried out by incubating with Rabbit TOM20 primary antibody followed by incubation with Alexa Fluor 555/647 goat antirabbit conjugate secondary antibody.

Coculture of BT474 and 3T3 Cells: BT474 cells were labeled with CellTracker Green CMFDA dye and 3T3 cells were labeled with CellTracker Deep Red dye. The cells were incubated for 24 h prior to administration of ND_{DOX} at concentrations of 25, 50, and 100 μg mL^{-1}. Each sample was analyzed on a confocal microscope after 24, 48, and 72 h of incubation with ND_{DOX}. The acquired images were processed with ImageJ to count the number of green cancer cells and white healthy fibroblasts in each sample.

Spheroids Culture: Spheroids containing BT474 breast cancer cells and 3T3 fibroblasts (3T3:BT474 at 1:1.5 ratio) were prepared using the hanging drop methodology. The spheroids were left to grow for 24 h and then transferred to a U-bottom 96-well plate and treated with NDDOX at 25 μg mL^{-1} for 72 h. After, the spheroids were fixed, included in optical cutting temperature (OCT) compound and sliced for immunofluorescence analysis at the confocal microscope.

3D Perfusion Cell Culture: BT474 and 3T3 cells with a seeding density of 350 000 cells were incubated with collagen scaffolds under static conditions for 3 days and then the scaffolds were assembled into U-cup perfusion flow bioreactor (Figure 7a) for another 4 days under continuous flow of cell culture media. The medium was replaced every 2 days. On the seventh day the medium was replaced with fresh medium containing 5, 10 and 25 μg mL^{-1} D_{DOX} and circulated for another 24 h. The bioreactor was then unassembled and the collagen scaffolds were retrieved to further process for cell viability using, CellTiter-Glo 3D, or fixed and included in OCT to be sliced for immunofluorescence, or H&E histological analysis.

Animal Studies: Female mice C57/BL6J with average weight 25 g aged 2 months were used in this study. Biosafety was assessed by injecting three animals with ND_{DOX} (2 mg ND_{DOX} kg^{-1}) at day 0 and the mice monitored for their activity and physical conditions over 10 days post-injection. Biodistribution studies were performed using ND_{DOX} particles radiolabeled with the short-lived and single photon γ-emitting isotope of indium-111 (^{111}In) and analyzed with γ-eye BIOEMTECH, at different time points. The protocols and all the animal procedures were approved by the General Directorate of Veterinary Services (Athens, Attica Prefecture, Greece) and by the Bioethical Committee of BIOEMTECH Laboratories (Permit number: EL 25 BIOexp 045) on the basis of the European Directive 2010/63/EU on the protection of animals used for experimental purposes. All animal procedures and in vivo studies were carried out by trained personnel at BIOEMTECH Laboratories.

Statistical Analysis: All results are shown as mean ± s.d. The statistical significance and *p* values were analyzed with Minitab 18 (Minitab LCC, Pennsylvania, USA) and Graphpad prism v.8.4.3 software, using one-way analysis of variance (ANOVA) with 95% confidence interval, Tukey's pairwise comparison, or two-way ANOVA followed by Bonferroni post-test.

Supporting Information

Supporting Information is available from the Wiley Online Library or from the author.

Acknowledgements

S.K.B. and S.F. contributed equally to this work. This work was supported by the Australian Research Council (ARC) under a Future Fellowship (F.C., FT140100873). F.C. acknowledges the award of a National Health and Medical Research Council Senior Principal Research Fellowship (GNT1135806). This work received funding from the European Union's Horizon 2020 research and innovation programme under the Marie Skłodowska-Curie Grant Agreement No. 690901 (NANOSUPREMI). G.F. acknowledges the European Social Fund and European Regional Development Fund-Project MAGNET (Number CZ.02.1.01/0.0/0.0/15_003/0000492). S.K.B. acknowledges the University of Melbourne for support through a Melbourne Research Scholarship and a Norma Hilda Schuster Scholarship. This work was performed in part at the Materials Characterisation and Fabrication Platform (MCFP) at the University of Melbourne. Marco Cassani, an iCARE-2 fellow, has received funding from Fondazione per la Ricerca sul Cancro (AIRC) and the European Union's horizon 2020 research and innovation programme under the Marie Skłodowska-Curie Grant Agreement No. 800924. The authors acknowledge Anshul Baral for his assistance with electron microscopy imaging and Helena Ďuríková for helping with the in vitro culture of iPSC-derived cardiomyocytes culture.

Open access publishing facilitated by RMIT University, as part of the Wiley - RMIT University agreement via the Council of Australian University Librarians.

Conflict of Interest

The authors declare no conflict of interest.

Data Availability Statement

The data that support the findings of this study are available from the corresponding author upon reasonable request.

Keywords

cancer therapy, mitochondria, nanodrugs, ultrasound

Received: October 5, 2021
Revised: January 24, 2022
Published online:

[1] a) S. E. McNeil, *Nat. Rev. Mater.* **2016**, *1*, 16073; b) S. Wilhelm, A. J. Tavares, Q. Dai, S. Ohta, J. Audet, H. F. Dvorak, W. C. W. Chan, *Nat. Rev. Mater.* **2016**, *1*, 16014.

[2] N. Kamaly, Z. Xiao, P. M. Valencia, A. F. Radovic-Moreno, O. C. Farokhzad, *Chem. Soc. Rev.* **2012**, *41*, 2971.

[3] a) E. Beltran-Gracia, A. Lopez-Camacho, I. Higuera-Ciapara, J. B. Velazquez-Fernandez, A. A. Vallejo-Cardona, *Cancer Nanotechnol.* **2019**, *10*, 11; b) C. L. Ventola, *P T* **2017**, *42*, 742.

[4] a) T. Sun, Y. S. Zhang, B. Pang, D. C. Hyun, M. Yang, Y. Xia, *Angew. Chem., Int. Ed. Engl.* **2014**, *53*, 12320; b) R. Misra, S. Acharya, S. K. Sahoo, *Drug Discovery Today* **2010**, *15*, 842; c) K. Ni, G. Lan, W. Lin, *ACS Cent. Sci.* **2020**, *6*, 842; d) Y. Yan, M. Bjornmalm, F. Caruso, *ACS Nano* **2013**, *7*, 9512.

[5] O. C. Farokhzad, R. Langer, *ACS Nano* **2009**, *3*, 16.

[6] J. Szebeni, D. Simberg, A. Gonzalez-Fernandez, Y. Barenholz, M. A. Dobrovolskaia, *Nat. Nanotechnol.* **2018**, *13*, 1100.

[7] a) M. Zhou, X. Zhang, Y. Yang, Z. Liu, B. Tian, J. Jie, X. Zhang, *Biomaterials* **2013**, *34*, 8960; b) Y. Liang, X. Fu, C. Du, H. Xia, Y. Lai, Y. Sun, *Artif. Cells, Nanomed., Biotechnol.* **2020**, *48*, 1114; c) C. Yu, M. Zhou, X. Zhang, W. Wei, X. Chen, X. Zhang, *Nanoscale* **2015**, *7*, 5683.

[8] X. Zhang, N. Li, S. Zhang, B. Sun, Q. Chen, Z. He, C. Luo, J. Sun, *Med. Res. Rev.* **2020**, *40*, 1754.

[9] S. K. Bhangu, G. Bocchinfuso, M. Ashokkumar, F. Cavalieri, *Nanoscale Horiz.* **2020**, *5*, 553.

[10] F. Cavalieri, E. Colombo, E. Nicolai, N. Rosato, M. Ashokkumar, *Mater. Horiz.* **2016**, *3*, 563.

[11] M. Ashokkumar, F. Cavalieri, F. Chemat, Y. Mizukoshi, K. Okitsu, A. Sambandam, K. Yasui, B. Zisu, *Handbook of Ultrasonics and Sonochemistry*, Springer, Singapore **2016**.

[12] K. Lemanska, H. Szymusiak, B. Tyrakowska, R. Zielinski, A. E. Soffers, I. M. Rietjens, *Free Radical Biol. Med.* **2001**, *31*, 869.

[13] S. Sindhwani, A. M. Syed, J. Ngai, B. Y. Maiorino, J. Rothschild, P. MacMillan, Y. W. Zhang, N. U. Rajesh, T. Hoang, J. L. Y. Wu, S. Wilhelm, A. Zilman, S. Gadde, A. Sulaiman, B. Ouyang, Z. Lin, L. S. Wang, M. Egeblad, W. C. W. Chan, *Nat. Mater.* **2020**, *19*, 566.

[14] A. Nel, E. Ruoslahti, H. Meng, *ACS Nano* **2017**, *11*, 9567.

[15] a) G. Petrangolini, R. Supino, G. Pratesi, L. Dal Bo, M. Tortoreto, A. C. Croce, P. Misiano, P. Belfiore, C. Farina, F. Zunino, *J. Pharmacol. Exp. Ther.* **2006**, *318*, 939; b) M. De Cesare, G. Pratesi, P. Perego, N. Carenini, S. Tinelli, L. Merlini, S. Penco, C. Pisano, F. Bucci, L. Vesci, S. Pace, F. Capocasa, P. Carminati, F. Zunino, *Cancer Res.* **2001**, *61*, 7189.

[16] D. Agudelo, P. Bourassa, G. Berube, H. A. Tajmir-Riahi, *Int. J. Biol. Macromol.* **2014**, *66*, 144.

[17] D. B. Sawyer, X. Peng, B. Chen, L. Pentassuglia, C. C. Lim, *Prog. Cardiovasc. Dis.* **2010**, *53*, 105.

[18] B. Cheregi, C. Timpani, K. Nurgali, A. Hayes, E. Rybalka, *Neuromuscular Disord.* **2015**, *25*, S202.

[19] D. G. Deavall, E. A. Martin, J. M. Horner, R. Roberts, *J. Toxicol.* **2012**, *2012*, 645460.

[20] a) F. Yang, S. S. Teves, C. J. Kemp, S. Henikoff, *Biochim. Biophys. Acta* **2014**, *1845*, 84; b) B. Jawad, L. Poudel, R. Podgornik, N. F. Steinmetz, W. Y. Ching, *Phys. Chem. Chem. Phys.* **2019**, *21*, 3877.

[21] a) F. Mollinedo, C. Gajate, *J. Lipid Res.* **2020**, *61*, 611; b) V. Ribas, C. Garcia-Ruiz, J. C. Fernandez-Checa, *Clin. Transl. Med.* **2016**, *5*, 5246; c) J. Montero, A. Morales, L. Llacuna, J. M. Lluis, O. Terrones, G. Basanez, B. Antonsson, J. Prieto, C. Garcia-Ruiz, A. Colell, J. C. Fernandez-Checa, *Cancer Res.* **2008**, *68*, 5246.

[22] a) J. A. Villa-Pulgarin, C. Gajate, J. Botet, A. Jimenez, N. Justies, M. R. Varela, A. Cuesta-Marban, I. Muller, M. Modolell, J. L. Revuelta, F. Mollinedo, *PLoS Neglected Trop. Dis.* **2017**, *11*, e0005805; b) F. Mollinedo, M. Fernandez, V. Hornillos, J. Delgado, F. Amat-Guerri, A. U. Acuna, T. Nieto-Miguel, J. A. Villa-Pulgarin, C. Gonzalez-Garcia, V. Cena, C. Gajate, *Cell Death Dis.* **2011**, *2*, e158.

[23] O. M. de Brito, L. Scorrano, *Nature* **2008**, *456*, 605.

[24] K. A. Sarosiek, T. Ni Chonghaile, A. Letai, *Trends Cell Biol.* **2013**, *23*, 612.

[25] S. Zhang, X. Liu, T. Bawa-Khalfe, L. S. Lu, Y. L. Lyu, L. F. Liu, E. T. Yeh, *Nat. Med.* **2012**, *18*, 1639.

[26] a) A. Papadimitropoulos, A. Scherberich, S. Guven, N. Theilgaard, H. J. A. Crooijmans, F. Santini, K. Scheffler, A. Zallone, I. Martin, *Eur. Cells Mater.* **2011**, *21*, 445; b) G. Cerino, E. Gaudiello, T. Grussenmeyer, L. Melly, D. Massai, A. Banfi, I. Martin,

F. Eckstein, M. Grapow, A. Marsano, *Biotechnol. Bioeng.* **2016**, *113*, 226.
[27] C. Hirt, A. Papadimitropoulos, M. G. Muraro, V. Mele, E. Panopoulos, E. Cremonesi, R. Ivanek, E. Schultz-Thater, R. A. Droeser, C. Mengus, *Biomaterials* **2015**, *62*, 138.
[28] F. Foglietta, G. C. Spagnoli, M. G. Muraro, M. Ballestri, A. Guerrini, C. Ferroni, A. Aluigi, G. Sotgiu, G. Varchi, *Int. J. Nanomed.* **2018**, *13*, 4847.
[29] a) S. Mitra, L. N. Nguyen, M. Akter, G. Park, E. H. Choi, N. K. Kaushik, *Cancers (Basel)* **2019**, *11*, 1030; b) D. Trachootham, J. Alexandre, P. Huang, *Nat. Rev. Drug Discovery* **2009**, *8*, 579.
[30] P. T. Schumacker, *Cancer Cell* **2006**, *10*, 175.
[31] a) B. Perillo, M. Di Donato, A. Pezone, E. Di Zazzo, P. Giovannelli, G. Galasso, G. Castoria, A. Migliaccio, *Exp. Mol. Med.* **2020**, *52*, 192; b) P. Storz, *Front. Biosci.* **2005**, *10*, 1881.
[32] S. Kumari, A. K. Badana, M. M. G. , S. G. , R. Malla, *Biomarker Insights* **2018**, *13*, https://doi.org/10.1177/1177271918755391.
[33] W. Deng, K. J. McKelvey, A. Guller, A. Fayzullin, J. M. Campbell, S. Clement, A. Habibalahi, Z. Wargocka, L. Liang, C. Shen, V. M. Howell, A. F. Engel, E. M. Goldys, *ACS Cent. Sci.* **2020**, *6*, 715.
[34] a) M. Han, M. R. Vakili, H. Soleymani Abyaneh, O. Molavi, R. Lai, A. Lavasanifar, *Mol. Pharm.* **2014**, *11*, 2640; b) S. R. Jean, D. V. Tulumello, C. Riganti, S. U. Liyanage, A. D. Schimmer, S. O. Kelley, *ACS Chem. Biol.* **2015**, *10*, 2007.
[35] J. Wang, J. Li, Y. Xiao, B. Fu, Z. Qin, *RCS Med. Chem.* **2020**, *11*, 858.
[36] L. Zhao, B. Zhang, *Sci. Rep.* **2017**, *7*, 44735.
[37] R. F. Henderson, W. E. Bechtold, M. A. Medinsky, J. P. Fischer, T. T. Lee, *Toxicol. Appl. Pharmacol.* **1988**, *95*, 515.